Inorganic Chemistry
Article
pubs.acs.org/IC

Novel Mixed Cobalt/Chromium Phosphate $NaCoCr_2(PO_4)_3$ Showing Spin-Flop Transition

Khalifa Souiwa,[†] Madhu Chennabasappa,[‡] Rodolphe Decourt,[‡] Mongi Ben Amara,[†] Mourad Hidouri,*[,†] and Olivier Toulemonde*[,‡]

[†]Faculté des Sciences 5019, Monastir, Tunisie

[‡]CNRS, Univ. Bordeaux, ICMCB, UPR 9048 F-33600, Pessac, France

ABSTRACT: We describe the synthesis and the crystallographic and magnetic properties of a novel $NaCoCr_2(PO_4)_3$ phosphate. A conventional solid-state reaction was used to obtain single-phase powders. A Rietveld analysis of powder X-ray diffraction data proposes an orthorhombic symmetry similar to α-$CrPO_4$-type structure in space group *Imma* with the following unit cell parameters: $a = 10.413(1)$ Å; $b = 13.027(1)$ Å; $c = 6.372(1)$ Å. The framework consists of PO_4 tetrahedra, $M(1)O_6$ ($M(1) = Cr$) octahedra, and $M(2)_2O_{10}$ ($M(2) = 0.5Cr+0.5Co$) binuclear unit of edge-sharing MO_6 octahedra. It can be described in terms of two building blocks: sheets consisting of corner-sharing $M(2)_2O_{10}$ units with PO_4 tetrahedra found parallel to the (b,c) plane, and chains made by corner-sharing CrO_6 octahedra and PO_4 tetrahedra running along the b axis. From the interconnection of the sheets and chains, a 3D rigid skeleton is formed, exhibiting two kinds of intersecting tunnel channels containing the Na^+ ions. The proposed structure derives from the α-$CrPO_4$-type structure considering a positive charge balance according to the equation $Cr^{3+} \rightarrow Co^{2+} + Na^+$, resulting in sodium countercation introduction within the unoccupied channels shown in the α-$CrPO_4$ framework. Temperature-dependent DC and AC magnetic susceptibility is indicative of a long-range magnetic ordering occurring at 32 K. Further, spin-flop transition sheds light on a chromium-based phosphate for the first time.

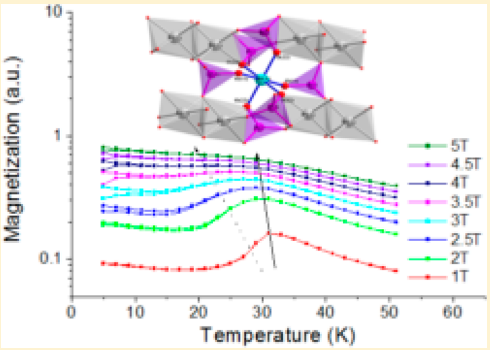

1. INTRODUCTION

Transition metal phosphates are extensively studied for their potential applications as ionic conductors,[1,2] nonlinear optics,[3−5] electrode materials for Li-ion batteries,[6,7] laser and piezoelectric materials,[8−10] and oxidative catalysts.[11−13] Despite early evidence in $FePO_4$[14] and $NaCoPO_4$[15] phases, fundamental interest in their unusual magnetic properties is more recent.[16,17]

Among the large number of existing phosphates, those containing chromium are scarce, being limited to the following compositions: $CrPO_4$,[18,19] $Cr_3(PO_4)_2$,[20] $Cr_7(PO_4)_6$,[21] $Na_3Cr_2(PO_4)_3$,[22] $Li_3TiCr(PO_4)_3$,[23] $MCr_4(PO_4)_6$ (M = Mg, Zn, Cu),[24] $Pb_3Cr_2(PO_4)_4$,[25] and $KBaCr_2(PO_4)_3$.[26] Their structures are built up from isolated CrO_6 octahedra,[22,23,25,26] bioctahedral units of edge-sharing Cr octahedra,[19,24] chains of edge-sharing CrO_6 octahedra,[19] or CrO_6 octahedra and CrO_5 trigonal bipyramids.[21] The phosphate groups serve as links for the Cr polyhedral units, giving rise to three-dimensional frameworks with tunnels and/or cavities available for the introduction of alkali and alkaline earth cations.

We are currently performing a systematic investigation of the Na_2O−*M*O−Cr_2O_3−P_2O_5 systems, where *M* is a divalent cation. This general study already led to the synthesis of $NaACr_2(PO_4)_3$ with A = Mg^{2+} or Zn^{2+} compounds showing a 3D long-range antiferromagnetic (AFM) ordering below 5 K. The long-range ordering is preceded by a short-range magnetic signal occurring at higher temperature and resulting from different strengths of magnetic exchange coupling between Cr^{3+} ions.[27] Ferrimagnetic material was proposed by substituting the diamagnetic divalent cation A (Mg^{2+} or Zn^{2+}) for a paramagnetic divalent one. Further, when Co^{2+} known to show spin−orbit-lattice coupling is considered, magnetic phase transitions might be expected.[28]

We report here our investigation of $NaCoCr_2(PO_4)_3$ and its unusual magnetic properties. The synthesis and powder X-ray diffraction methodology are described first prior to a depiction of the magnetic properties in close relation to crystallographic studies.

2. EXPERIMENTAL SECTION

2.1. Synthesis and Post Synthesis Elemental Analysis. $NaCoCr_2(PO_4)_3$ was synthesized in the powder form by a direct, solid state reaction starting from a stoichiometric mixture of reactants of analytical grade Na_2CO_3, $Co(NO_3)_2\cdot 3H_2O$, $Cr(NO_3)_3\cdot 9H_2O$, and $(NH_4)H_2PO_4$. This mixture was dissolved into aqueous acid solution and stirred prior to heating at 353 K to evaporate water. The resulting dry powder was placed in a platinum crucible, and a subsequent five step heat treatment from 473 to 1273 K was then performed over 24 h. The product was quenched to room temperature at each step of the heat treatment and intimately ground in an agate mortar prior to the

Received: April 16, 2015
Published: July 10, 2015

DOI: 10.1021/acs.inorgchem.5b00776
Inorg. Chem. 2015, 54, 7345−7352

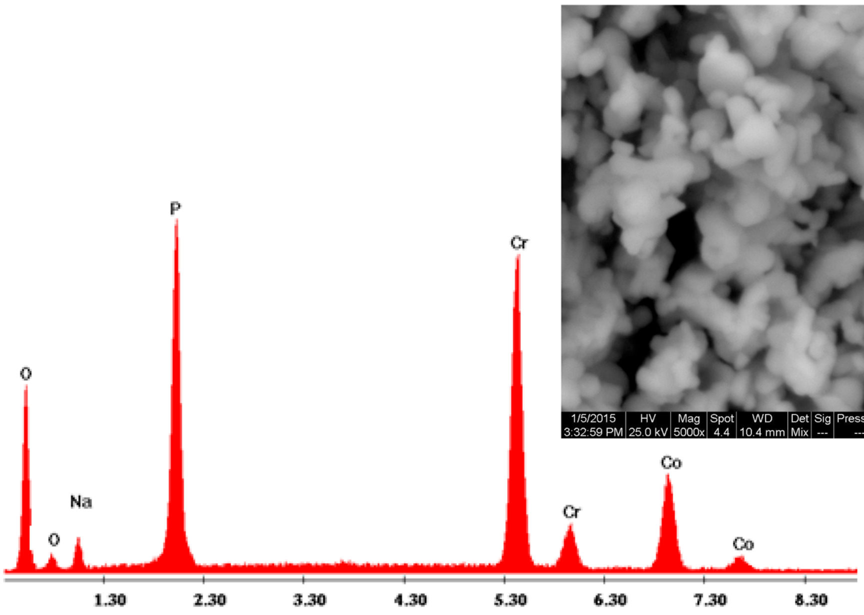

Figure 1. EDS spectrum and SEM micrograph (inset) of $NaCoCr_2(PO_4)_3$.

next step. In the final heat treatment, the product was kept twice at 1423 K over 24 h in air with one intermediate grinding. The dark green resulting powder was analyzed by X-ray powder diffraction to ensure the crystallographic purity. To compare the targeted chemical composition with the appropriate one, a semiquantitative analysis of the powder was performed by energy dispersive X-ray spectroscopy (EDS) mounted on a JEOL JSM6335F microscopy scanning electron microscope. The EDS spectrum shown in Figure 1 reveals the presence of Na, Co, Cr, and P elements. Micrographs of this powder are shown in the inset.

2.2. Powder X-ray Diffraction. For a complete structural analysis, the powder diffraction patterns were recorded at room temperature on a PANalytical X'Pert PRO diffractometer using monochromatic Cu K_α radiation (λ = 1.5406 Å) and operating in Bragg−Brentano geometry. Data were collected in the 2θ range of 10−120° with a step size of 0.008° and a dwell time of 2 s per step. The monophasic nature of the patterns and their relation to the α-$CrPO_4$-type structure was verified by the High-Score plus database.[29] Using the FULLPROF program,[31] a full pattern refinement was first carried out followed by a Rietveld analysis.[30] Because of the similarity between the title compound and the α-$CrPO_4$-like phosphate $NaV_3(PO_4)_3$,[32] the cell parameters, the space group, and the atomic positions established for the vanadium phosphate from single crystal X-ray data refinement were used as starting sets in the mixed cobalt/chromium pattern refinement procedure. Initially, the 2θ zero, a six degree polynomial function for the background, the unit cell lattice parameters, and the patterns profiled with a Pseudo−Voigt function were subsequently refined. Finally, the positional parameters, the site occupation factors, and individual isotropic parameters were allowed to refine. The goodness of the refinements was estimated by the residuals (R values), which converged at R_p = 1.6%, R_{wp} = 2.2%, and χ^2 = 4.9. The crystal data and experimental conditions for structural refinement are presented in Table 1.

2.3. Additional Characterization. Magnetic measurements were performed by a Quantum Design SQUID MPMS-XL magnetometer using fine powder of the crystals (49 mg) sealed in a gelatin capsule. The DC magnetic susceptibility was extracted from data acquired in the presence of 100 Oe magnetic fields on both zero-field-cooled (ZFC) and field-cooled (FC) conditions at temperatures fixed by the settle mode in the 5−300 K temperature range. The magnetization measurements were performed between 5 and 50 K in an applied field ranging in the 1−5 T range at both ZFC and FC conditions. Isothermal magnetizations were probed in the 0−4 T range on both increasing and decreasing applied magnetic field mode. Frequency-dependent AC susceptibility measurements at 10 Oe static magnetic fields and an applied oscillating magnetic field (H_{AC}) of 1 Oe were performed between 27 and 40 K (on heating mode) at frequencies (f) of 0.3, 33, 66, 111, 222, 330, and 997 Hz.

Table 1. Crystal Data and Structure Refinement Parameters for $NaCoCr_2(PO_4)_3$

formula unit	$NaCoCr_2(PO_4)_3$
crystal system	orthorhombic
space group	*Imma*
a /Å	10.411(1)
b /Å	13.028(1)
c /Å	6.376(1)
V /Å^3	864.8(1)
Z	4
angular range	(10° ≤ 2θ ≤ 120°)
step scan increment	0.008°
zero point	0.0183(1)
pseudo-Voigt function [PV = ηL + (1 − η)G]	η = 0.959(1)
no. of refined parameters	41
asymmetry parameter	0.1449(1)
pref. orientation parameter	1.022(1)
R_p	1.6
R_{wp}	2.2
R_{exp}	1.0
χ^2	4.9
R_B	14.0
R_F	15.8

Specific heat measurements were performed using a Quantum Design PPMS with a pellet of the product (17.6 mg). The data were acquired in the 5−50 K temperature range without any applied magnetic field in cooling and heating processes and in an applied magnetic field of 2.5 T at both ZFC and FC conditions.

3. RESULTS AND DISCUSSION

3.1. X-ray Studies. X-ray diffraction patterns for the $NaCoCr_2(PO_4)_3$ material are shown in Figure 2. As already discussed, this compound belongs to the family of compounds crystallizing within the related α-$CrPO_4$-type structure, namely, the phosphates $SrFe_3(PO_4)_3$,[17,34] $NaV_3(PO_4)_3$,[32] $RhPO_4$,[33] and

DOI: 10.1021/acs.inorgchem.5b00776
Inorg. Chem. 2015, 54, 7345−7352

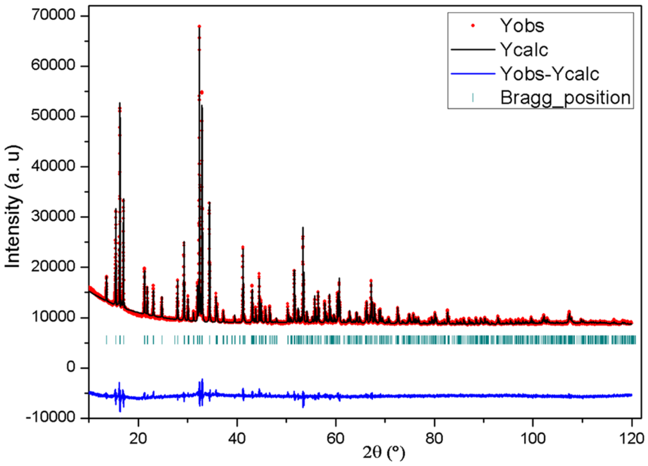

Figure 2. X-ray powder diffraction pattern for $NaCoCr_2(PO_4)_3$. The observed intensity data are depicted; the solid line overlying them is the calculated pattern. Vertical markers below the diffraction pattern indicate positions of Bragg reflections. Differences between observed and calculated intensities are plotted at the bottom using the same scale.

$Na_{1.28}Ni_{0.86}Fe_2(PO_4)_3$,[35] or the arsenates α-$CrAsO_4$[36] and $K_{1.250}Ni_{0.875}Fe_2(AsO_4)_3$.[37] At the initial stage of our refinement, one starts to refine the atomic positions considering those proposed by Kinomura et al. for $NaV_3(PO_4)_3$,[32] showing similarities with α-$CrPO_4$-type structure as described on the experimental section. Taking into account the Co/Cr ratio equal to 1:2 for the studied material, three kinds of cation distributions were envisaged: (1) the isolated octahedral site M(1) is fully occupied by the Co ion and the dimeric site M(2) by chromium atoms; (2) the isolated octahedral site M(1) is fully occupied by the Cr ion, and the dimeric site M(2) is shared with Cr and Co atoms; (3) a totally disordered distribution in both sites is considered (i.e., both sites are shared with Cr and Co and the sites occupancies are fixed to maintain the positive/negative charge balance. The best agreement between the calculated and observed patterns resulting in reasonable *R* values is obtained for the (2) distribution; there, only one mixed Co/Cr site is observed (labeled M(2)), whereas the other site (labeled M(1)) is exclusively occupied by Cr. Finally, individual isotropic parameters (B_{iso}) were refined. Refinement leads to correct values except for that of the O(12) site, which converges to a somewhat larger value than those of the remaining oxygen atoms. However, an alternative test of refinements either by fixing this parameter to the reasonable value of 1.0 or by splitting this site over two positions were unsuccessful.

Table 2 gives the final refined positional and thermal parameters. Further, the relevant interatomic distances are listed in Table 3. The asymmetric unit contains nine atomic positions, including one for Na, one for Cr (labeled M(1)), one mixed Co/Cr site (labeled M(2)), two for P, and four for O. All these sites are located on special positions at inversion centers or 2-fold axes, except for O(21) and O(22), which occupy general positions of space group *Imma*. The 3D framework is built up of $M(1)O_6$ and $M(2)O_6$ octahedra and PO_4 tetrahedra. The Cr and P polyhedra are isolated from each other while each pair of M(2) octahedra share a common edge to form an $M(2)_2O_{10}$ bioctahedral unit.

Although complex, the framework shown in Figures 3 and 4 can be easily described considering the association of two building blocks: (1) The $M(2)_2O_{10}$ units are based on pairs of edge-sharing octahedra linked by $P(1)O_4$ tetrahedra through common oxygen corners. Their interconnection forms sheets in the *bc* plane. (2) The chains running parallel to the *b*-axis are made by corner-sharing $M(1)O_6$ octahedra and $P(2)O_4$ tetrahedra. The alternate stacking of these two building blocks along the *a* direction induces two kinds of intersecting tunnels parallel to the *a* and *b* directions, where the Na^+ ions are located (Figure 4). These tunnels communicate through six-sided windows, showing the opened character of the structure.

The polyhedral environments of the $M(2)_2O_{10}$ unit and the $M(1)O_6$ octahedron are depicted in Figure 5. The $M(2)_2O_{10}$ unit (Figure 5a) shares six of its corners with six PO_4 tetrahedra and two edges with two other tetrahedra; the four oxygen atoms forming these edges are also shared with four CrO_6 octahedra. The M(2)−O distances range from 2.054(4) Å to 2.074(4) Å (Table 3) with a mean distance <M(2)−O> = 2.062 Å, in good agreement with Co^{2+} (*r*[6] = 0.745 Å) or Cr^{3+} (*r*[6] = 0.615 Å) ionic radii (*r*[6] = 0.615 Å). The mean distance <M(2)−O> indeed ranges between 1.972 Å, observed for Cr^{3+} ion in α-$CrPO_4$,[36] and 2.168 Å, reported for Co^{2+} with the same coordination in $NaCoPO_4$.[15] The Brown bond valence sum[37] equal to +2.41 further suggests a mixture of Cr^{3+} and Co^{2+} ions. Each $M(1)O_6$ octahedron shares all of its corners with PO_4 tetrahedra, four of these corners also being shared with four $M(2)_2O_{10}$ units (Figure 5b). This octahedron is also distorted, as seen from the M(1)−O distances scattering from 1.987(1) to 2.042(1) Å with a mean distance of 2.005(1) Å, close to 1.971(1) Å reported for octahedral Cr^{3+} ions in α-$CrPO_4$.[36]

The P−O distances within the two distinct PO_4 tetrahedra show a large discrepancy (from 1.479(1) to 1.582(1) Å), indicating their high degree of distortion. However, the main distances <P(1)−O> = 1.514(1) Å and <P(2)−O> = 1.533(1) Å, and their the respective bond valence sum (5.28 for P(1)

Table 2. Atomic Coordinates and Isotropic Thermal Displacement Parameters for $NaCoCr_2(PO_4)_3$

site	Wyckoff	atom	*x*	*y*	*z*	B_{iso} (Å^2)
Na	4e	Na	0	1/4	0.4078(9)	1.944(2)
M(1)	4a	Cr	0	0	0	0.108(7)
M(2)	8g	0.5Cr + 0.5Co	1/4	0.6336(1)	1/4	0.349(4)
P(1)	4e	P	0	1/4	0.9157(7)	0.869(2)
P(2)	8g	P	1/4	0.4258(4)	1/4	0.227(7)
O(11)	8h	O	0	0.6546(4)	0.9471(8)	0.372(2)
O(12)	8i	O	0.8852(5)	1/4	0.7714(2)	1.412(2)
O(21)	16j	O	0.2132(3)	0.3630(3)	0.4336(5)	0.112(2)
O(22)	16j	O	0.1363(3)	0.5053(3)	0.2179(5)	0.666(2)

DOI: 10.1021/acs.inorgchem.5b00776
Inorg. Chem. 2015, 54, 7345−7352

Table 3. Main Interatomic Distances in $NaCoCr_2(PO_4)_3$

			$M(1)O_6$		
M(1)−O(22)	×4	1.987(1)	O(11)−M(1)−O(22)	×4	94.65(3)
M(1)−O(11)	×2	2.042(1)	O(11)−M(1)−O(22)	×4	85.35(3)
<M(1)−O>		2.005(1)	O(22)−M(1)−O(22)	×2	88.88(3)
			O(22)−M(1)−O(22)	×2	91.12(2)
			O(11)−M(1)−O(11)		179.96(5)
			O(22)−M(1)−O(22)	×2	180.00(3)
			$M(2)O_6$		
M(2)−O(21)	×2	2.054(1)	O(12)−M(2)−O(12)		86.01(3)
M(2)−O(22)	×2	2.059(1)	O(12)−M(2)−O(21)	×2	85.54(3)
M(2)−O(12)	×2	2.074(1)	O(12)−M(2)−O(21)	×2	92.64(3)
<M(2)−O>		2.062(1)	O(12)−M(2)−O(22)	×2	101.34(2)
			O(21)−M(2)−O(22)	×2	90.46(2)
			O(21)−M(2)−O(22)	×2	91.56(2)
			O(12)−M(2)−O(12)		71.44(2)
			O(12)−M(2)−O(22)	×2	172.23(3)
			O(21)−M(2)−O(21)		177.52(3)
			$P(1)O_4$		
P(1)−O(12)	×2	1.508(1)	O(12)−P(1)−O(12)		104.80(1)
P(1)−O(11)	×2	1.520(1)	O(12)−P(1)−O(11)	×4	110.55(1)
<P(1)−O>		1.514(1)	O(11)−P(1)−O(11)		105.1(2)
			$P(2)O_4$		
P(2)−O(21)	×2	1.479(1)	O(21)−P(2)−O(21)		112.78(2)
P(2)−O(22)	×2	1.587(1)	O(21)−P(2)−O(22)		105.68(2)
<P(2)−O>		1.533(1)	O(21)−P(2)−O(22)	×2	116.90(2)
			O(21)−P(2)−O(22)		105.68(2)
			O(22)−P(2)−O(22)		98.48(2)
			NaO_8		
Na−O(11)	×2	2.581(1)			
Na−O(12)	×2	2.609(1)			
Na−O(21)	×4	2.669(1)			
<Na−O>		2.632(1)			

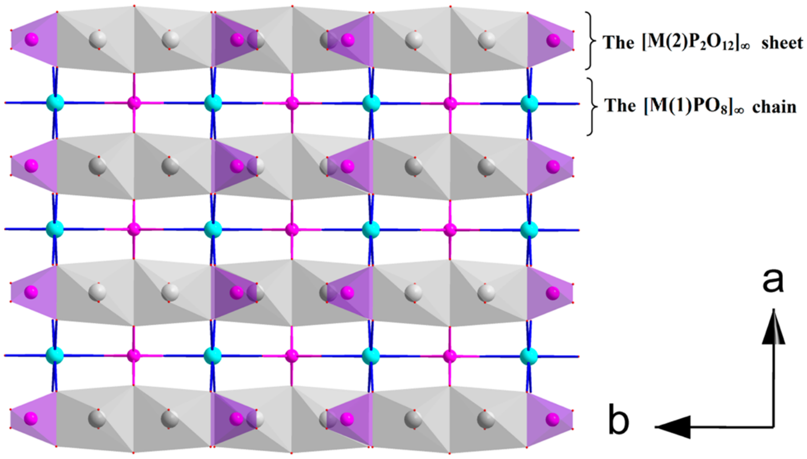

Figure 3. $[CoCr_2(PO_4)_3]_\infty$ framework.

and 5.07 for P(2)), are typical of those observed in the α-$CrPO_4$[36] structure (<P(1)−O> = 1.530(1) Å resulting in B.V.S = 5.08, and <P(2)−O> = 1.542(1) Å resulting in B.V.S = 5.18) and more generally in monophosphates.[38]

The environment of the Na^+ ions was determined assuming cation−oxygen distances below the limit L_{max} = 3.12 Å suggested by Donnay and Allman.[39] This environment consists of eight oxygen atoms with Na−O distances between 2.581(1) and 2.669 Å, forming a highly distorted cubic environment as seen in related phosphates.[32,39,40]

3.2. Magnetic Properties. The temperature dependencies of the molar magnetic susceptibility and the inverse molar magnetic susceptibility both corrected from the diamagnetic signal (-190.10^{-6} emu/mol) for the mixed cobalt/chromium phosphate are plotted in Figure 6.

A paramagnetic to antiferromagnetic phase transition is shown at T_N = 35 ± 5 K. The ordering temperature is on the same order of magnitude but slightly higher than those observed for the isostructural α-$CrPO_4$,[36] $NaACr_2(PO_4)_3$ (A = Mg, Zn),[27] and $NaCoPO_4$,[15] but slightly lower than that shown

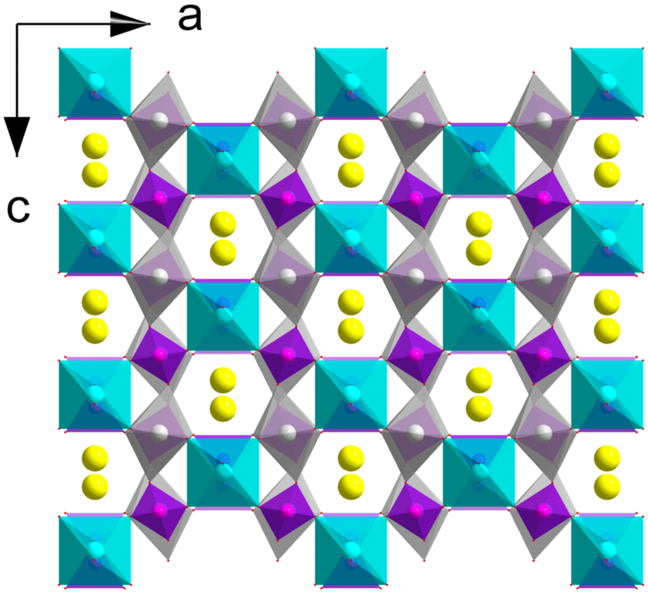

Figure 4. A projection along the [010] direction of the $NaCoCr_2(PO_4)_3$ structure showing the sodium countercations located in the tunnel.

for $SrFe_3(PO_4)_3$.[17,34] An upturn on cooling after the antiferromagnetic transition related to the thermal hysteresis between ZFC and FC mode is unambiguously seen. Such an upturn of the magnetization coupled with the thermal hysteresis was not observed in our previous study on $NaACr_2(PO_4)_3$ (A = Mg, Zn) or in the α-$CrPO_4$ compound,[36] whereas a sharp increase in the magnetization is seen on $SrFe_3(PO_4)_3$.[17] The paramagnetic state is noticed only for a temperature >100 K. For such a high range of temperatures, the magnetic susceptibility data obey the Curie−Weiss law, giving a Curie−Weiss constant $\theta = -62$ K and a Curie constant C of 6.79 emu K mol^{-1} (or a paramagnetic moment μ_{eff} of 7.37 μ_B). They range between those calculated from a spin-only hypothesis for both Cr^{3+} and Co^{2+} cations ($C = 5.625$ emu K mol^{-1} or $\mu_{eff} = 6.71$ μ_B) and those calculated from a spin-only

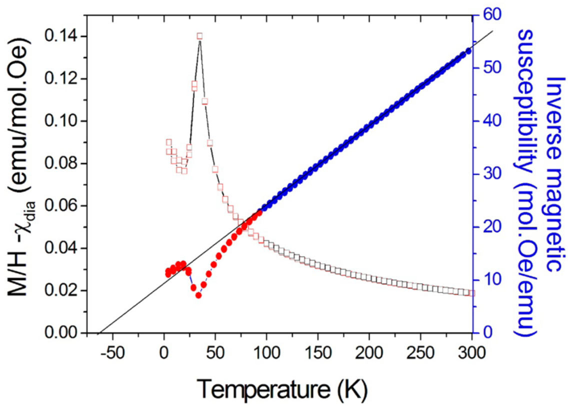

Figure 6. Magnetic susceptibility and inverse magnetic susceptibility versus temperature for $NaCoCr_2(PO_4)_3$. The solid line highlights the range of temperature for which a Curie−Weiss law is supported.

hypothesis for Cr^{3+} and with accurate treatment considering an unquenched orbital contribution and a spin−orbit coupling for Co^{2+} ($C = 9.24$ emu K mol^{-1} or $\mu_{eff} = 8.60$ μ_B). Thus, the experimental paramagnetic moment suggests a non-negligible orbital contribution, as expected for Co^{2+} cations.[42,43] Indeed, if the expected experimental paramagnetic signal is subtracted from the two Cr^{3+} ions within a spin-only hypothesis, as observed for $NaACr_2(PO_4)_3$ (A = Mg, Zn)[27] and α-$CrBO_4$ (B = P and As)[36] compounds, one can estimated the paramagnetic signal carried by the cobalt cation in $NaCoCr_2(PO_4)_3$ to be $\mu_{eff} = 4.93$ μ_B. Such a value is fully consistent with those reported by Lopez and co-workers for the same octahedra environment and close average Co−O distances.[43] Further, the negative Curie−Weiss constant indicating that the antiferromagnetic interactions dominate is also supported by the deviation of inverse magnetic susceptibility below the Curie−Weiss limit on cooling toward the antiferromagnetic phase transition. Such unusual behavior on the magnetic short-range domain is also shown in the α-$CrPO_4$ compound.[36] It was already pointed out for $Ba_{n+1}Co_nO_{3n-1}Br$ (n = 5 and 6) compounds showing a spin-flop transition.[41]

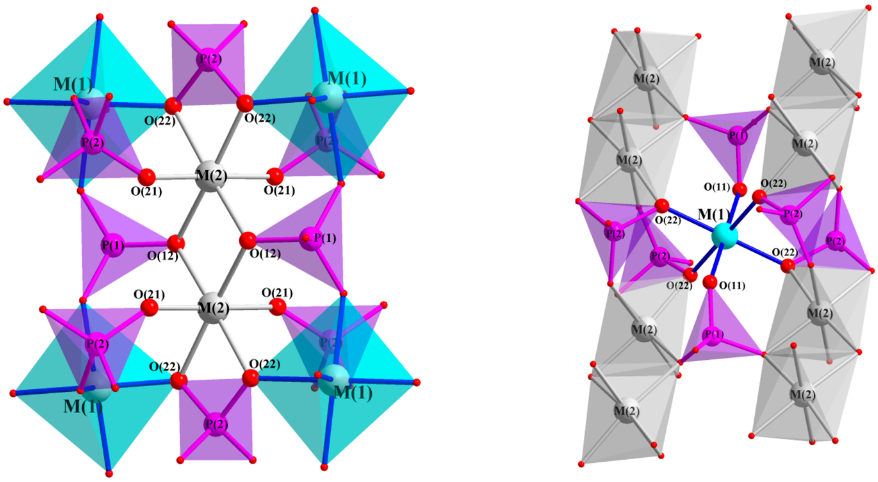

(a) Polyhedral environments of the M_2O_{10} unit

(b) Polyhedral environments of the $M(1)O_6$ octahedron

Figure 5. Polyhedral environments.

Because it was proposed that $SrFe_3(PO_4)_3$ undergoes to re-entrant spin glass transition at low temperature,[17] AC magnetic susceptibility was studied and plotted in Figure 7, and magnetization at increasing magnetic field from 1 to 5 T was studied and plotted in Figure 8.

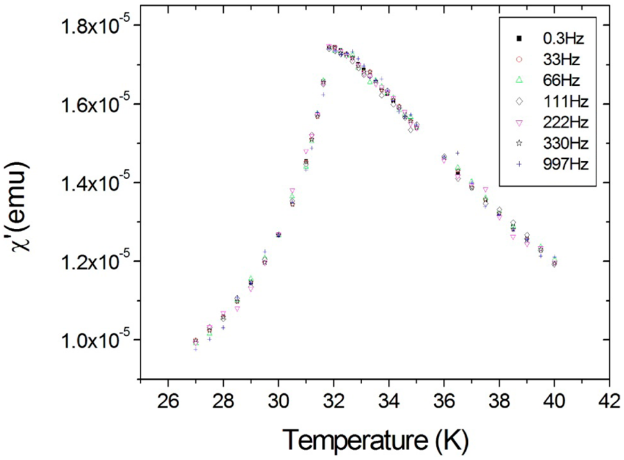

Figure 7. Variation of AC real part of magnetic susceptibility with temperature.

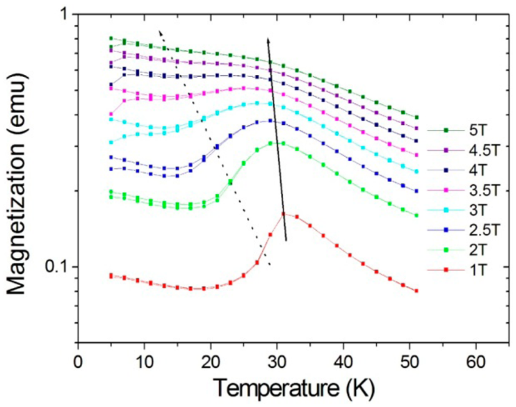

Figure 8. Temperature dependence of the magnetization measured at different applied fields from 1 to 5 T on both ZFC and FC modes. Arrows are a guide for the eyes to discriminate the applied field amplitude dependence of the two magnetic features.

There is no obvious shift of peak intensities and/or positions. The in-phase $\chi'(T)$ is clearly frequency independent, supporting a long-range magnetic ordering. The magnetic transition is quite sharp and occurs at T_N = 31.8 ± 0.2 K following a rounded shape, indicating short-range magnetic interactions are likely in $M(2)_2O_{10}$ (M(2) = 0.5 Cr + 0.5 Co) bioctahedral units, as discussed in the previous paragraph and seen in our temperature-dependent electron paramagnetic resonance study for $NaACr_2(PO_4)_3$ (A = Mg, Zn) compounds.[27] The not shown, out-of-phase $\chi''(T)$ signal is very low and noisy, suggesting that its amplitude is out of the range of measurement. The phase transition is likely made without any dissipation. Interestingly, the magnetization is not frequency independent but is highly sensitive to the amplitude of the magnetic excitation field, as illustrated in Figure 9. First, from the local maximum unambiguously seen on the second derivative of the temperature dependence of the magnetization, the antiferromagnetic state is still observed at 5 T. That maximum slightly shifts toward lower temperature when the magnetic excitation field increases, as pointed out by the solid line arrow to reach 29 K at 5 T. Second, the dot line arrow indicates the critical magnetic field which induces a spin-flop transition at lower temperature than the long-range ordering. It is noticeable that the thermal hysteresis between ZFC and FC mode pertains to the spin-flop transition temperature range. It further supports the long-range ordering character of the first magnetic transition. Such thermal hysteresis is likely related to dynamic effects. Figure 9 summarizes the final (H,T) phase diagram deduced from the systematic M(T) and M(H) (not shown) screening of the system.

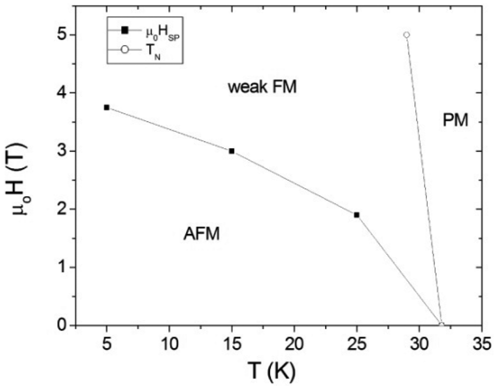

Figure 9. H,T magnetic phase diagram built from the experimental data (temperature dependence of the magnetization (circle dot) and isothermal magnetization versus magnetic field (square dot)). AFM, antiferromagnetic phase; weak FM, weak ferromagnetic phase resulting from the spin-flop transition; PM, paramagnetic phase. Solid lines are guides for the eyes.

3.5. Specific Heat Measurements. To gain a better understanding of the magnetic phase transition, we measured the applied magnetic field and temperature dependence of the specific heat for $NaCoCr_2(PO_4)_3$ phosphate. Plotted in Figure 10 is the data collected over the same temperature range as the temperature dependence of the magnetization shown in Figure 8. Interestingly, the curves nicely match outside of the temperature range of the magnetic transition, and no thermal hysteresis is observed on both sets of data collected using different experimental conditions (with and without an applied

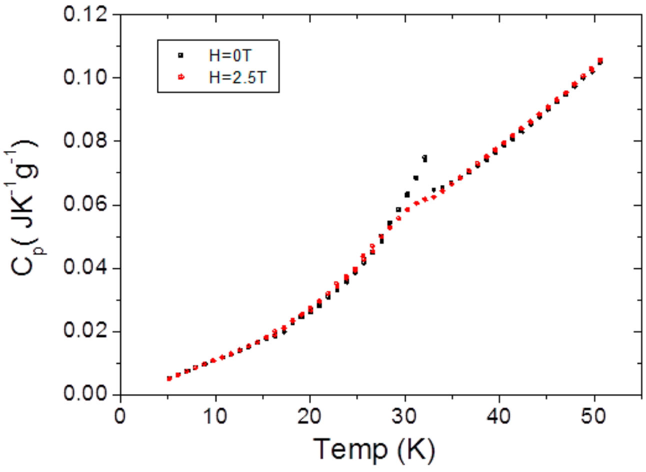

Figure 10. Specific heat versus temperature data collected without any magnetic field and at 2.5 T for $NaCoCr_2(PO_4)_3$.

magnetic field). The specific heat data collected at 0 T exhibits a lambda shape peak. It indicates a magnetic long-range ordering, and with the absence of any hysteresis, suggests a second order magnetic transition. The lambda shape peak appears at a similar temperature (32 ± 1.0 K) as that of the magnetic phase transition observed in the AC magnetic susceptibility data. When a magnetic field is applied, the specific heat is gradually extinguished, and only a tiny noticeable feature is observed at 2.5 T. From the second derivative temperature dependence, the peak transition is still observed, and as expected, slightly shifted toward a lower temperature (31 ± 1.0 K at 2.5 T). Such behavior (persistence of the anomaly but becoming attenuated in magnitude, broadened, and shifted to lower temperatures) is typical from an antiferromagnetic order that is destabilized by an external stimulus (i.e., the magnetic field).[44,45]

The spin-flop transition can be discussed according to semiempirical Goodenough–Kanamori–Anderson rules. From the crystallographic study, two sets of Superexchange interactions coexist and compete. The first set is found considering the M(1)–O(22)–M(2) superexchange interactions with M(1) = Cr and M(2) = 0.5 Cr + 0.5 Co. From Figure 4b, four such magnetic ion-ligand O(22)-magnetic-ion interactions occur in CrO_6 octahedron, whereas the two others oxygen atoms labeled O(11) are shared with the PO_4 group. The magnetic ion-ligand O(22)-magnetic-ion angle is 120°, which is relatively far from 180°. Despite this discrepancy in angle, it results in 180° superexchange interactions, which are strongly antiferromagnetic for Cr^{3+}-O(22)-Cr^{3+} but weakly ferromagnetic for Co^{2+}-O(22)-Cr^{3+}. The second set of superexchange interactions is found within the $M(2)_2O_{10}$ (M(2) = 0.5 Cr + 0.5 Co) dimeric units. Within a $Co(2)_2O_{10}$ unit, 90° ferromagnetic superexchange interactions are expected, in contrast with 90° antiferromagnetic superexchange interactions in a $Cr(2)_2O_{10}$ unit as seen[27] in $NaMCr_2(PO_4)_3$ with M = Mg^{2+} and Zn^{2+}. Furthermore, direct exchange interactions within the $M(2)_2O_{10}$ via the t_{2g} orbitals and M(1)-O(11)–O(12)–M(2) and M(1)–O(22)–O(21)–M(2) superexchange interactions via $P(1)O_4$ and $P(2)O_4$ groups, respectively, cannot be excluded. The fact that a local maximum at 29 K on the temperature dependence of the magnetization measured at 5 T is still observed unambiguously suggests that the spin-flop transition is still not fully completed and that the dominant superexchange interactions are the 180° superexchange interactions, which are strongly antiferromagnetic for Cr^{3+}–O(22)–Cr^{3+}. However, joint temperature and magnetic field dependence powder neutron diffraction and/or density functional theory calculations and/or high magnetic field experiments would confirm the magnetic ground state and estimate all the magnetic coupling between direct, separated first and second transition metal atoms and the relaxed exchange energies per unit.[46]

4. CONCLUSIONS

$NaCoCr_2(PO_4)_3$ was synthesized by the solid state reaction and characterized by X-ray diffraction, AC and DC magnetic susceptibility, and specific heat measurements. This compound displays a structure analogous to the α-$CrPO_4$ type. It consists of a 3D framework built up by PO_4 tetrahedra, $M(1)O_6$ octahedra, and $M(2)_2O_{10}$ (M(2) = 0.5 Cr + 0.5 Co) bioctahedral units of edge-sharing $M(2)O_6$ octahedra. The Na^+ ions are located within intersecting tunnels delimited by the framework. The magnetic susceptibility and the specific heat reveal a magnetic phase transition from para- to antiferromagnetic behavior at ~32 K. Further, a spin-flop transition is highlighted, likely due to the competition within the M_2O_{10} bioctahedral units between Co^{2+}–O(2p)–Cr^{3+} ferromagnetic 90° superexchange interactions and Cr^{3+}–O(2p)–Cr^{3+} antiferromagnetic 90° superexchange interactions and mediated by direct exchange. The long-range magnetic ground state is supported by the strong antiferromagnetic superexchange interactions for Cr^{3+}–O(22)–Cr^{3+}.

AUTHOR INFORMATION

Corresponding Authors

*E-mail: mourad_hidouri@yahoo.fr.
*E-mail: olivier.toulemonde@icmcb.cnrs.fr.

Notes

The authors declare no competing financial interest.

ACKNOWLEDGMENTS

M.C. acknowledges the Université de Bordeaux for a Ph.D. fellowship.

REFERENCES

(1) Hagman, L. O.; Kierkegaard, P. *Acta Chem. Scand.* **1968**, *22*, 1822–1832.

(2) Goodenough, J. B.; Hong, H. Y. P; Kafalas, J. A. *Mater. Res. Bull.* **1976**, *11*, 203–220.

(3) Zumsteg, F. C.; Bierlein, J. D.; Gier, T. E. *J. Appl. Phys.* **1976**, *47*, 4980–4985.

(4) Stucky, G. D.; Phillips, M. L. F.; Gier, T. E. *Chem. Mater.* **1989**, *1*, 492–509.

(5) Runkel, M. J.; De Yoreo, J. J.; Sell, W. D.; Milam, D. *Proc. SPIE* **1997**, *3244*, 51–63.

(6) Padhi, A. K.; Nanjundaswany, K. S.; Goodenough, J. B. *J. Electrochem. Soc.* **1997**, *144*, 1188–1194.

(7) Padhi, A. K.; Nanjundaswany, K. S.; Masquelier, C.; Goodenough, J. B. *J. Electrochem. Soc.* **1997**, *144*, 2581–2586.

(8) Danielmeyer, H. G.; Weber, H. P. *IEEE J. Quantum Electron.* **1972**, *8*, 805–808.

(9) Weber, H. P.; Damen, T. C.; Danielmeyer, H. G.; Tofield, B. C. *Appl. Phys. Lett.* **1973**, *22*, 534–536.

(10) Cambon, O.; Haines, J.; Fraysse, G.; Detaint, J.; Capelle, B.; Van-der-Lee, A. *J. Appl. Phys.* **2005**, *97*, 074110/1–074110/7.

(11) Cora, F.; Catlow, C. R. A.; D'Ercole, A. *J. Mol. Catal. A: Chem.* **2001**, *166*, 87–99.

(12) Cavani, F.; Trifiro, F. *Chem. Rev.* **1988**, *88*, 18–24.

(13) Subrahmanyam, C.; Viswanathan, B.; Varadarajan, T. K. *J. Mol. Catal. A: Chem.* **2004**, *223*, 149–153.

(14) Battle, P. D.; Cheetham, A. K.; Gleitzer, C.; Harrison, W. T. A.; Long, G. J.; Longworth. *J. Phys. C: Solid State Phys.* **1982**, *15*, L919–L924.

(15) Feng, P.; Bu, X.; Stucky, G. D. *J. Solid State Chem.* **1997**, *131*, 160–166.

(16) David, R.; Pautrat, A.; Filimonov, D.; Kabbour, H.; Vezin, H.; Whangbo, M -H; Mentré, O. *J. Am. Chem. Soc.* **2013**, *135*, 13023–13029.

(17) Shang, M. Y.; Chen, Y.; Tian, G.; Yuan, H. M.; Feng, S. H. *Phys. B* **2013**, *409*, 42–46.

(18) Glaum, R.; Gruehn, R.; Moeller, M. *Z. Anorg. Allg. Chem.* **1986**, *543*, 111–116.

(19) Attfield, J.-P.; Battle, P. D.; Cheetham, A. K. *J. Solid State Chem.* **1985**, *57*, 357–361.

(20) Glaum, R.; Schmidt, A. *Z. Anorg. Allg. Chem.* **1997**, *623*, 1672–1678.

(21) Glaum, R. *Z. Kristallogr.* **1993**, *205*, 69–83.

(22) Genkina, E. A. *Kristallografiya* **1991**, *36*, 1126–1130.

(23) Patoux, S.; Rousse, G.; Leriche, J.-B.; Masquelier, C. *Solid State Sci.* **2004**, *6*, 1113−1120.
(24) Gruss, M.; Glaum, R. *Z. Kristallogr.* **1997**, *212*, 510.
(25) Palkina, K. K.; Saifuddinov, V. Z.; Lavrov, A. V. *Dokl. Akad. Nauk SSSR* **1977**, *237*, 1090−1093.
(26) Battle, P. D.; Gibb, T. C.; Nixon, S. *J. Solid State Chem.* **1988**, *75*, 21−29.
(27) Souiwa, K.; Hidouri, M.; Toulemonde, O.; Duttine, M.; Amara, M. B. *J. Alloys Compd.* **2015**, *627*, 153−160.
(28) Neilson, J. R.; Morse, D. E.; Melot, B. C.; Shoemaker, D. P.; Kurzman, J. A.; Seshadri, R. *Phys. Rev. B: Condens. Matter Mater. Phys.* **2011**, *83*, 094418−1 - 094418−7.
(29) *X'Pert HighScore Plus (PW3212)*, version 2.0; PANalytical B.V., 2003.
(30) Rietveld, H. M. *Acta Crystallogr.* **1967**, *22*, 151−152.
(31) Rodriguez-Carvajal, J. *FullProf*, version 1.9c; Mai, LLB 2001.
(32) Kinomura, N.; Matsui, N.; Kumada, N.; Muto, F. *J. Solid State Chem.* **1989**, *79*, 232−237.
(33) Rittner, P.; Glaum, R. *Z. Kristallogr.* **1994**, *209*, 162−169.
(34) Korzenski, M. B.; Kolis, J. W.; Long, G. J. *J. Solid State Chem.* **1999**, *147*, 390−398.
(35) Hidouri, M.; Lajmi, B.; Driss, A.; Amara, M. B. *J. Chem. Crystallogr.* **2004**, *34*, 669−672.
(36) Attfield, J.-P.; Battle, P. D.; Cheetham, A. K. *Inorg. Chem.* **1989**, *28*, 1207−1213.
(37) Brown, I. D.; Altermatt, D. *Acta Crystallogr., Sect. B: Struct. Sci.* **1985**, *41*, 244−247.
(38) Baur, W. H. *Acta Crystallogr., Sect. B: Struct. Crystallogr. Cryst. Chem.* **1974**, *30*, 1195−1215.
(39) Donnay, G.; Allman, R. *Am. Mineral.* **1970**, *55*, 1003−1015.
(40) Essehli, R.; Belharouak, I.; Ben Yahia, H.; Chamoun, R.; Orayech, B.; El Bali, B.; Bouziane, K.; Zhou, X. L.; Zhou, Z. *Dalton Trans.* **2015**, *44*, 4526−4532.
(41) Toulemonde, O.; Roussel, P.; Isnard, O.; André, G.; Mentré, O. *Chem. Mater.* **2010**, *22*, 3807−3816.
(42) Melot, B. C.; Drewes, J. E.; Seshadri, R.; Stoudenmire, E. M.; Ramirez, A. P. *J. Phys.: Condens. Matter* **2009**, *21*, 216007−216014.
(43) Lopez, C. A.; Saleta, M. E.; Curiale, J.; Sanchez, R. D. *Mater. Res. Bull.* **2012**, *47*, 1158−1163.
(44) Fisher, R. A.; Radhakrishna, P.; Phillips, N. E.; Badding, J. V.; Stacy, A. M. *Phys. Rev. B: Condens. Matter Mater. Phys.* **1995**, *52*, 13519−13525.
(45) Alfonso, B. F.; Piqué, C.; Trobajo, C.; García, J. R.; Kampert, E.; Zeitler, U.; Fernández, J. R.; Fernández-Díaz, M. T.; Blanco, J. A. *Phys. Rev. B: Condens. Matter Mater. Phys.* **2010**, *82*, 144431−144431−10.
(46) Zhang, Y.; Kan, E.; Xiang, H.; Villesuzanne, A.; Whangbo, M. *Inorg. Chem.* **2011**, *50*, 1758−1166.